

ARTICLE

<https://doi.org/10.1038/s41467-019-10856-z>

OPEN

High efficiency perovskite quantum dot solar cells with charge separating heterostructure

Qian Zhao^{1,2,3}, Abhijit Hazarika², Xihan Chen², Steve P. Harvey², Bryon W. Larson², Glenn R. Teeter², Jun Liu², Tao Song², Chuanxiao Xiao², Liam Shaw⁴, Minghui Zhang¹, Guoran Li³, Matthew C. Beard² & Joseph M. Luther²

Metal halide perovskite semiconductors possess outstanding characteristics for optoelectronic applications including but not limited to photovoltaics. Low-dimensional and nanostructured motifs impart added functionality which can be exploited further. Moreover, wider cation composition tunability and tunable surface ligand properties of colloidal quantum dot (QD) perovskites now enable unprecedented device architectures which differ from thin-film perovskites fabricated from solvated molecular precursors. Here, using layer-by-layer deposition of perovskite QDs, we demonstrate solar cells with abrupt compositional changes throughout the perovskite film. We utilize this ability to abruptly control composition to create an internal heterojunction that facilitates charge separation at the internal interface leading to improved photocarrier harvesting. We show how the photovoltaic performance depends upon the heterojunction position, as well as the composition of each component, and we describe an architecture that greatly improves the performance of perovskite QD photovoltaics.

¹ College of Chemistry, Nankai University, 300071 Tianjin, China. ² National Renewable Energy Laboratory, Golden, CO 80401, USA. ³ Institute of New Energy Chemistry Material, Nankai University, 300350 Tianjin, China. ⁴ Warren Wilson College, Asheville, NC 28815, USA. Correspondence and requests for materials should be addressed to J.M.L. (email: joey.luther@nrel.gov)

Heterostructures within optoelectronic devices offer unique control of the electron and hole energy levels throughout the device^{1–3}. For example, in photovoltaic (PV) devices, energy band engineering can enable better harvesting of photo-generated charge carriers^{4–6}. This concept is especially prevalent in vapor deposited heterostructures using MOCVD and MBE of III–V semiconductors⁷ as well as in sputtered or thermally evaporated systems such as CIGS where the composition at surfaces can be altered to promote a buried location for the actual *p-n* charge separating junction^{8,9}. In solution processed metal halide perovskite semiconductors, such a concept has not been successfully demonstrated primarily due to there being no existing pathway to prevent the solvation of the first deposited perovskite layer by the solvent of the subsequently deposited perovskite layer. In contrast, for perovskite QD films, the solvent does not technically dissolve the precursor materials, but rather suspends the QDs by their surface ligands in a colloidal solution. In layer-by-layer deposition of perovskite QD films, a layer of QDs is deposited from the colloidal solution and then ligands are chemically removed, rendering the resulting film insoluble to the nonpolar solvent, thus, enabling the ability to process the subsequent QD-layers without affecting the underlying film^{10–12}. In our standard process, a QD-colloid in hexane or octane contains perovskite QDs terminated with organic ligands and is first deposited onto the desired substrate. The resulting QD film is treated with methyl acetate (MeOAc) that effectively removes native oleate ligands¹². A second QD deposition can then be applied and the ligand removal process is repeated. In principle, the second (or any subsequent) solution can contain either the same QDs or QDs of different composition allowing for the composition of the perovskite film to be modulated in almost any desired order throughout the film thickness.

Results

Demonstration of heterojunction. To demonstrate the compositional heterojunction (schematically shown in Fig. 1a) as described above, we employ time-of-flight secondary ion mass spectrometry (ToF-SIMS) depth profiling¹³ on various films prepared herein (Fig. 1b–d). The SIMS detects signals for Cs, formamidinium (FA), Pb, I, Ti, and In while sputtering through the film using an ion beam¹³. First, a pure CsPbI₃ QD film on TiO₂ is characterized and the Cs, Pb and I signals of the QD film are observed in the ToF-SIMS depth profile. (Fig. 1b) At roughly 300 nm into the film, a sharp rise of the Ti signal becomes prominent indicating the ion beam has reached the underlying TiO₂ layer. In Fig. 1c, we show ToF-SIMS for a heterostructured film containing CsPbI₃ QDs deposited on top of Cs_{0.25}FA_{0.75}PbI₃ QDs. At roughly 200 nm into the film, the Cs signal decreases slightly while the FA signal rises (Fig. 1c). The distinct and sharp interface (rising several orders of magnitude) seen here with ToF-SIMS is nearly as sharp as the CsPbI₃ interface with TiO₂ in such a sample. In Fig. 1d, the perovskite compositions of the film structure are reversed compared to Fig. 1c, and here it is clear that a similar interface is formed within the film stack with the diminishment of the FA signal along with a slight increase in the Cs signal. This indicates a clear interface between layers of QDs with different compositions is formed and the sequence of these two QD layers can also be controlled via layer-by-layer deposition. In Supplementary Fig. 1 we show using ToF-SIMS that the integrity of such heterojunctions is minimally compromised after aging or moderate heating.

Optical and electronic properties. The successful construction of perovskite heterostructured films allows the investigation of the resulting composite optoelectronic properties. First, the electronic

properties of the heterostructure are studied with X-ray photoelectron and ultraviolet photoelectron spectroscopies (XPS and UPS) to probe energy band positions in films of each QD composition (see Methods and Supplementary Fig. 2 for details and analysis). In Fig. 2a, we plot the resulting energy level positions for each QD film. The measured energy levels indicate that a higher FA content leads to deeper conduction band edges, valence-band edges, and Fermi level positions relative to vacuum. Thus, there is an opportunity to create an energy offset that could drive electrons towards a layer containing more FA while holes are driven toward layers with less FA. The band positions for spiro-OMeTAD, TiO₂ and contacts are also shown in Fig. 2a for reference.

Next, we determine how the macroscopic optical properties of the films are controlled by the varying thickness and composition of each layer. It has been previously shown that perovskite QD devices with ~300-nm-thick perovskite QD films have optimized power conversion efficiencies (PCEs)^{10,14,15}. To be consistent, we perform a 4-cycle spin-coating procedure which, due to the QD concentration and solution properties, leads to a perovskite QD film with a total thickness of ~300 nm. Figure 2b presents the external quantum efficiency (EQE) of PV devices as a function of the internal heterostructure interface position of the Cs_{0.25}FA_{0.75}PbI₃ portion to that of CsPbI₃. Two main features to note are the systematic shift in the absorption onset from 720 nm for pure CsPbI₃ films to 790 nm for a film containing only Cs_{0.25}FA_{0.75}PbI₃ and a reduction in the collection efficiency of blue wavelengths for the devices containing higher amounts of FA within the film. In addition, the effect of changing the composition of lower-bandgap bottom layer in EQE is also investigated and presented in Fig. 2c. The composition of the bottom layer again causes a systematic shift in the absorption onset of the composite film but is less dramatic than observed in Fig. 2b.

Device design and performance. Given the optical properties of the heterojunction-containing films and the energetics shown above, Fig. 3 presents PV performance of the corresponding devices. Using the device architecture shown in Fig. 3a, a series of solar cells were fabricated (EDS elemental mapping of the cross section and morphology of QDs presented in Supplementary Figs. 3 and 4, respectively). Figure 3b shows *J-V* curves for devices to investigate the impact of thickness ratio of Cs_{0.25}FA_{0.75}PbI₃ layer to CsPbI₃ layer in the perovskite QD absorber. However, since we observe non-negligible hysteresis during the reverse and forward scans of devices (shown in Supplementary Fig. 5), the power conversion efficiency (PCE) from stabilized power output (SPO) at 0.950 V is reported (Fig. 3c). This figure of merit (PCE from SPO) has now become required for accurate reporting of efficiency for perovskite solar cells^{16,17}. The reproducibility of these devices is demonstrated by showing the histograms of PCE from SPO (Supplementary Fig. 6). Despite similar PCE from the reverse scans for several devices, the device containing layer ratio of 1:3 (Cs_{0.25}FA_{0.75}PbI₃: CsPbI₃) has the highest PCE of 15.52% (see Table 1 and parameters from the forward scans presented in Supplementary Table 1 as well as heterojunction layer and device stability in the Supplementary Figs. 1 and 7). The improvement is mainly attributed to increased *J_{sc}* and suggests more photogenerated charge carriers are harvested with this architecture¹⁸. As a control experiment, devices from simply blending the two QD solutions at the same ratio (1:3 Cs_{0.25}FA_{0.75}PbI₃: CsPbI₃) were also prepared (Supplementary Fig. 8). It is anticipated that this would form more of a bulk heterojunction architecture rather than the planar heterojunction films described here. These bulk heterojunction QD devices show

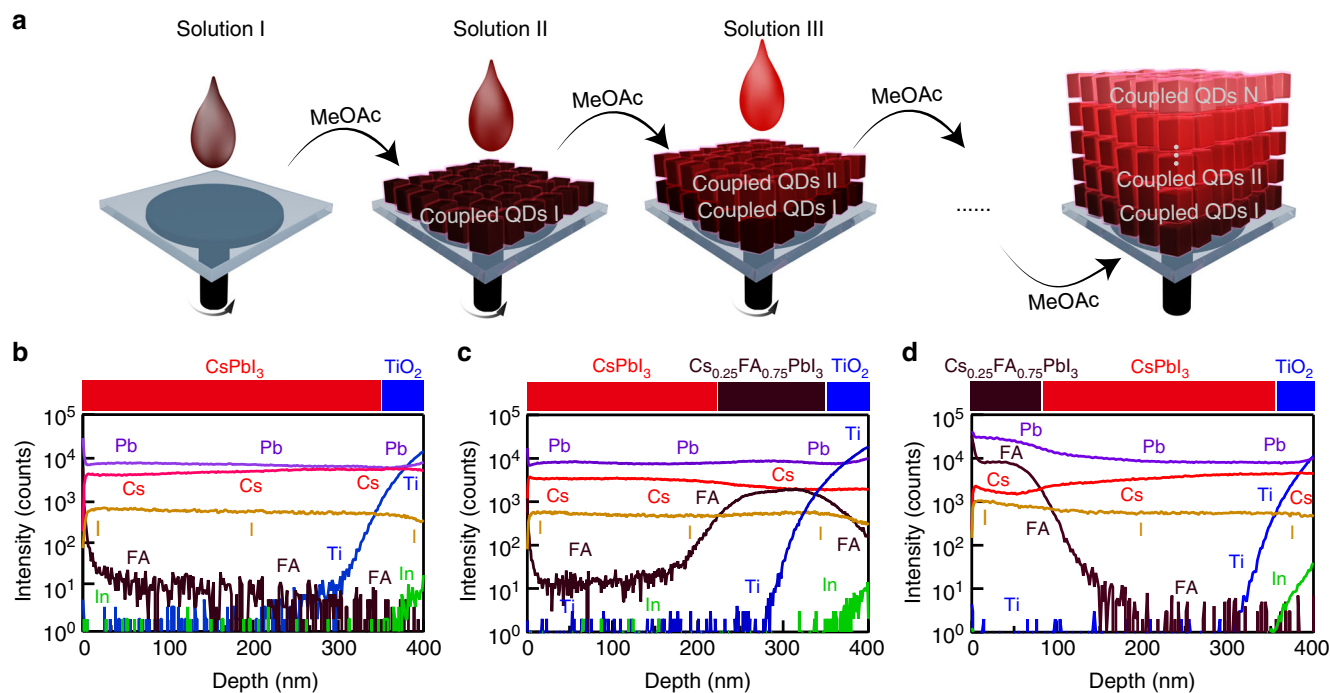


Fig. 1 Heterojunction structure of QD films. **a** Schematic overview of layer-by-layer assembly showing a perovskite QD film composed of different layers of QDs. MeOAc treatment is carried out between the deposition of different QD layers to remove the native oleate ligands and to render the deposited QDs insoluble in the solvent. **b–d** ToF-SIMS depth profile of samples with the structure and interface location indicated in the bar above the plots of CsPbI₃/TiO₂ (**b**), CsPbI₃/Cs_{0.25}FA_{0.75}PbI₃/TiO₂ (**c**), and Cs_{0.25}FA_{0.75}PbI₃/CsPbI₃/TiO₂ (**d**). All relevant elements from perovskite QD layer and TiO₂ are shown. Compared to the structure without Cs_{0.25}FA_{0.75}PbI₃, the FA signal shows a sharp and significant change and the Cs signal also shows a slight change at the boundary between the CsPbI₃ and Cs_{0.25}FA_{0.75}PbI₃ QD layers. The In signal is shown as a reference for when the ToF-SIMS profiling beam reaches the ITO on the substrate

characteristics similar to single component devices rather than the improved carrier harvesting seen in planar heterojunction devices.

Time-resolved carrier dynamics of heterojunction films. To rationalize the high PCE of perovskite/perovskite QD heterojunctions, the mobility and lifetime of photogenerated carriers in each QD film were obtained using time-resolved microwave conductivity (TRMC). We find the carriers in the more FA-containing films possess longer free-carrier lifetimes but also exhibit lower effective mobility compared to pure CsPbI₃ QD films (Supplementary Fig. 9). In other words, the trade-off in lower carrier mobility for longer average carrier lifetime results in increased recombination and less charge collection for thick FA-containing layers. Consequently, we observe a decrease in FF and J_{sc} for the devices with excessively thick FA-containing layers. This also helps to explain the reduction of EQE shown for 350 to 550 nm wavelengths in Fig. 2b. Light with wavelength around 450 nm is primarily absorbed in the FA-containing heterojunction component and shows poorer collection in thicker FA-containing layers. In Fig. 3d, e, we present J - V curves and SPO for devices with different compositions of the lower bandgap layer in the heterojunction with the optimized heterojunction position determined from Fig. 3c. There is negligible difference for device performance when the bottom-most layer of the absorber is Cs_{0.75}FA_{0.25}PbI₃, Cs_{0.5}FA_{0.5}PbI₃, Cs_{0.25}FA_{0.75}PbI₃, or FAPbI₃ (see Supplementary Table 2), which may be associated with the slightly different energy levels and that the fast charge separation is similar in each case.

To better understand the charge separation dynamics induced by the designed heterojunction, we performed transient

absorption (TA) spectroscopy which can independently probe carrier populations in each component of the heterojunction upon illumination. In the TA spectra (presented as pseudocolor images, Fig. 4) near the bandgap energy, a reduced absorption (ground state bleach) generally corresponds to the presence of excitons or free-charge carriers and the center of the reduced absorption indicates the exciton transition energy¹⁹. In Fig. 4 we show TA data for a heterojunction film excited at 400 nm either through the high bandgap CsPbI₃ side (Fig. 4a) or through the lower bandgap Cs_{0.25}FA_{0.75}PbI₃ side (Fig. 4c) as well as single component films of each composition (Fig. 4f, g). The anticipated energy band diagram is shown in Fig. 4b, indicating a 180-meV conduction band offset that will drive electrons towards the FA-containing component. The valence-band offset favors hole transfer to CsPbI₃ but has only a small energetic offset of 20 meV, which is less than kT at room temperature, thus holes will mainly diffuse in the heterostructure. The TA spectra cannot be represented by only one bleaching component and we model our data by a sum of two Gaussian peaks, one centered at 697 nm and corresponds to carriers residing in the CsPbI₃ component and another centered at 728 nm corresponding to carriers residing in the Cs_{0.25}FA_{0.75}PbI₃ component. In Fig. 4a, a strong bleach is mainly observed at 697 nm due to excitation into the CsPbI₃ component. As the delay between the pump and probe beam is swept between 1 ps and 2000 ps, the bleach component at 697 nm is transferred to one at 728 nm due to electron transfer from CsPbI₃ to Cs_{0.25}FA_{0.75}PbI₃. In Fig. 4d, the fractional component of the bleach in each component is plotted versus delay time and we find that initially 80% of the bleach is composed of that attributed to the CsPbI₃ while ~20% initially penetrates through the CsPbI₃ to Cs_{0.25}FA_{0.75}PbI₃. The fractional component in the

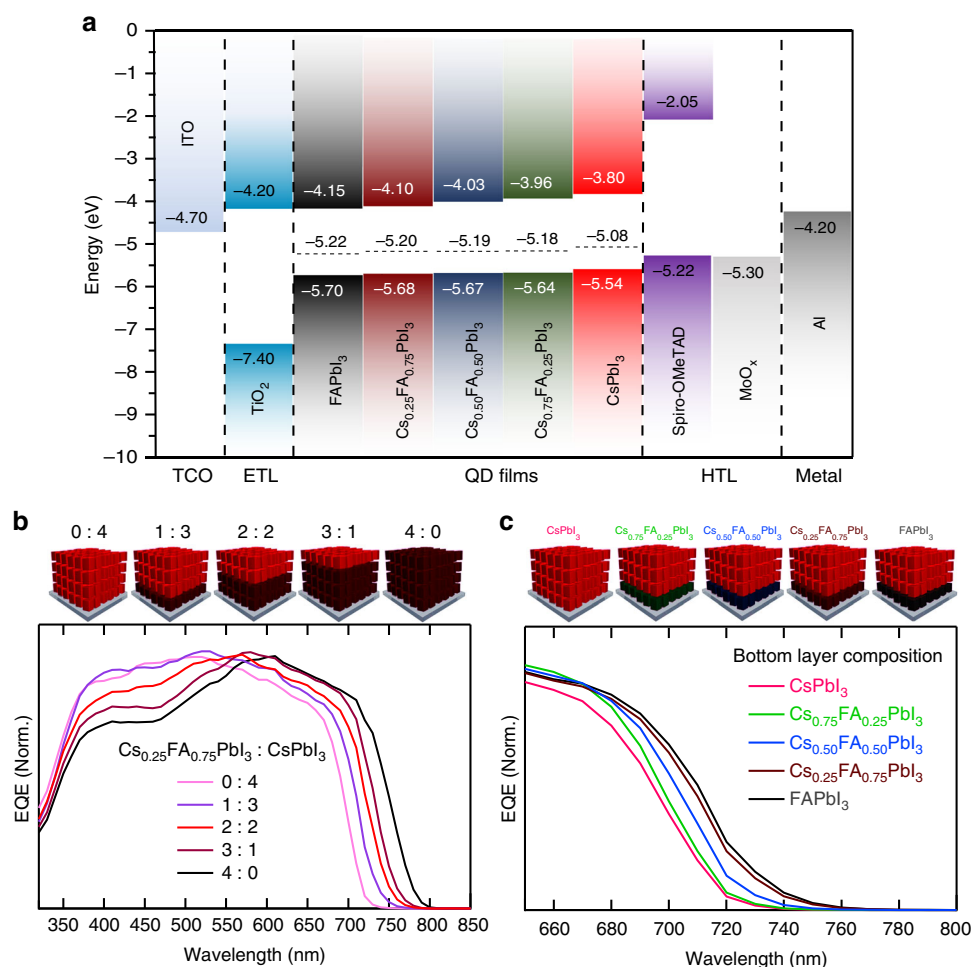


Fig. 2 Optical and electronic properties of perovskite QD heterojunction. **a** Energy band positions for perovskite QD compositions and contact layers considered in this work. The Fermi level positions (denoted by horizontal dotted lines) and valence-band edges (E_v) of all perovskite QD films were determined by UPS and XPS, respectively. The conduction band edges (E_c) were calculated by adding the bandgap energy²⁶ to E_v for the corresponding perovskite QD films. **b** EQE spectra of solar cells with varying thickness ratio of the $\text{Cs}_{0.25}\text{FA}_{0.75}\text{PbI}_3$ layer to CsPbI_3 layer in the perovskite QD absorber. **c** EQE spectra of solar cells with different compositions of the bottom layer in the perovskite QD absorber where the thickness ratio of the mixed-cation $\text{Cs}_x\text{FA}_{1-x}\text{PbI}_3$ QD layers to CsPbI_3 QD layers is 1:3 in all cases

CsPbI_3 decreases with time with a characteristic electron transfer time of ~ 600 ps. Such induced charge separation is advantageous for suppressing recombination and enhancing charge extraction^{20,21}.

In Fig. 4e, the fractional components are plotted when the film is instead excited through the $\text{Cs}_{0.25}\text{FA}_{0.75}\text{PbI}_3$ side. Again, about 20% of the excitation is transmitted through the $\text{Cs}_{0.25}\text{FA}_{0.75}\text{PbI}_3$ to the CsPbI_3 back layer in this case and the bleach signal remains roughly constant with time. In the lower panel in Fig. 4a, c, selected line cuts from the surface plots are shown along with component Gaussian fits to better visualize the charge transfer. The selected cuts in Fig. 4a show the increasing component of the bleach growing in at 153 ps and 1865 ps relative to 1.48 ps after excitation. In Fig. 4c, initially at 1.48 ps, a small 20% component of the bleach is due to the CsPbI_3 layer as discussed but this signal decreases with increased pump-probe delay since TA has been shown to be more sensitive to electron than hole signatures²² and a much lesser driving force for hole transfer as indicated in the band diagram.

We also performed TA for pure single component CsPbI_3 QD and pure $\text{Cs}_{0.25}\text{FA}_{0.75}\text{PbI}_3$ (shown in Fig. 4f, g, respectively). These single component films show a bleach at 688 nm for CsPbI_3

QDs and 738 nm for the $\text{Cs}_{0.25}\text{FA}_{0.75}\text{PbI}_3$ sample which do not evolve much with time. These spectra are provided for reference. As explained by this TA analysis, charge transfer inside the absorber induced by heterojunction efficiently separates photo-generated electrons and (to a lesser degree) holes driving them opposite directions.

Discussion

We develop perovskite devices that enables the rational design of charge separating interfaces within a perovskite QD absorber layer. By controlling the QD composition during layer-by-layer QD-film deposition, we can locate a spatial heterostructure arbitrarily within the resulting perovskite layer. We show how the composition of each heterostructure-component can be optimized based on charge-carrier lifetimes and mobilities within each component-QD to achieve a PCE from SPO up to 15.74%. Our concept could be easily employed with QDs and other forms of absorber layers (thin films¹⁵, 2D structures²³, or combinations therein²⁴). Furthermore, our approach should lead to a larger design-space which will impact a wider range of perovskite-based optoelectronic applications such as LEDs, transistor, (spintronic or quantum information processing, etc.).

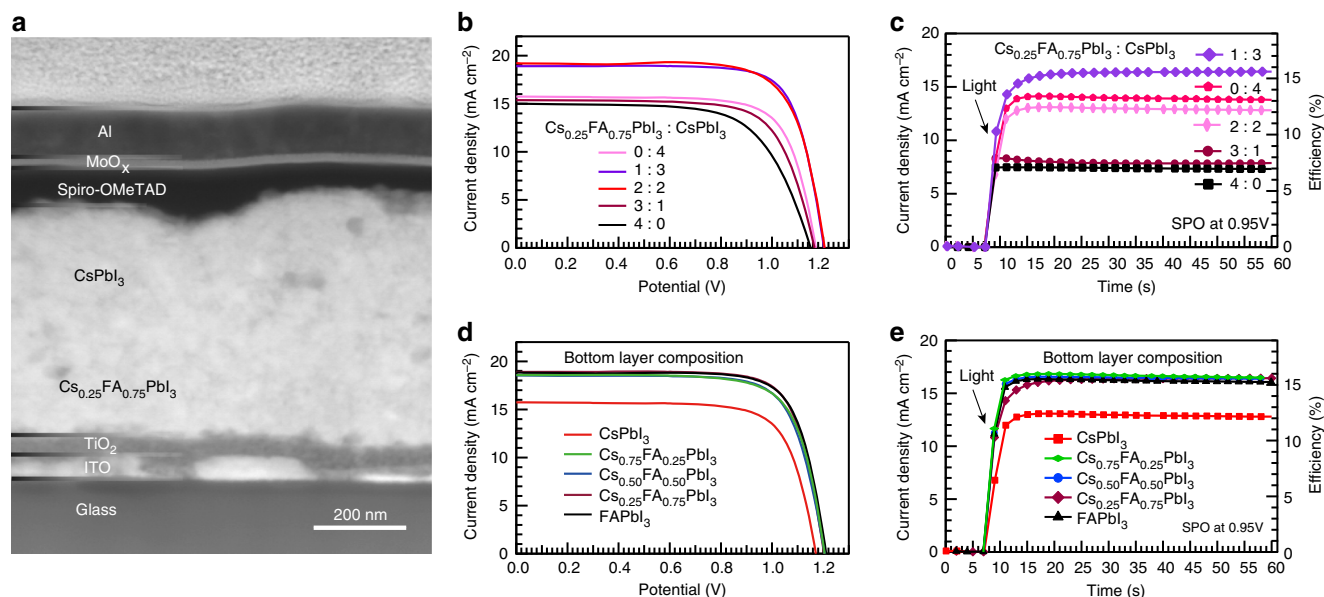


Fig. 3 Photovoltaic performance of solar cells. **a** Cross-sectional STEM-HAADF image of devices with the structure of Glass/ITO/TiO₂/Cs_{0.25}FA_{0.75}PbI₃/CsPbI₃/spiro-OMeTAD/MoO_x/Al. **b, c** *J-V* curves recorded by reverse scans (from open circuit to short circuit) and SPO at 0.95 V of devices with different thickness ratio of Cs_{0.25}FA_{0.75}PbI₃ layer to CsPbI₃ layer in the perovskite QD absorber, respectively. **d, e** *J-V* curves measured via reverse scans and SPO at 0.95 V of devices with different compositions of the bottom layer in the perovskite QD absorber where the heterojunction position is constant

Table 1 Photovoltaic parameters of solar cells

Thickness ratio (Cs _{0.25} FA _{0.75} PbI ₃ : CsPbI ₃)	V _{oc} (V)	J _{sc} (mA cm ⁻²)	FF (%)	PCE (%)	SPO (%)
0:4	1.17	15.75	74	13.67	12.15
1:3	1.20	18.91	76	17.39	15.52
2:2	1.21	19.21	74	17.16	13.11
3:1	1.17	15.37	72	12.84	7.45
4:0	1.15	14.99	66	11.43	6.94

J-V parameters from reverse scans and conversion efficiency of devices with different thickness ratio of Cs_{0.25}FA_{0.75}PbI₃ layer to CsPbI₃ layer in the perovskite QD absorber

Methods

Materials. Formamidinium iodide (CH(NH₂)₂, FAI) was purchased from Dyesol. Lead (II) iodide (PbI₂; 99.9985%) and bis(trifluoromethane)sulfonimide lithium salt (Li-TFSI) were purchased from Alfa Aesar. 2,2',7,7'-tetrakis(*N,N*-di-*p*-methoxyphenylamino)-9,9'-spirobifluorene (spiro-OMeTAD; ≥99.5%) was purchased from Lumtec. Cesium carbonate (Cs₂CO₃; 99.9%), oleylamine (OAm; technical grade, 70%), oleic acid (OA; technical grade, 90%), 1-octadecene (ODE; technical grade, 90%), octane (anhydrous, ≥99%), hexane (reagent grade, ≥95%), methyl acetate (MeOAc; anhydrous, 99.5%), lead nitrate (Pb(NO₃)₂; 99.999%), ethyl acetate (EtOAc; anhydrous, 99.8%), formamidinium acetate (FA-acetate, 99%), titanium ethoxide (≥97%), hydrochloric acid (HCl; 37% in water), chlorobenzene (anhydrous, 99.8%), 4-tert-butylpyridine (4-TBP; 96%), toluene (anhydrous, 99.8%), dimethylformamide (DMF), dimethyl sulfoxide (DMSO), and acetonitrile (anhydrous, 99.8%) were purchased from Sigma-Aldrich and used as received unless otherwise specified.

CsPbI₃ QDs synthesis and purification. The synthesis was performed following the method reported in our previous publications with slight modification^{11,25}. First, 0.407 g of Cs₂CO₃ was added in 20 mL of ODE containing 1.25 mL of OA and degassed at 150 °C for 20 min under vacuum in a 100-mL three-neck flask. After Cs₂CO₃ was absolutely dissolved in the solution, the Cs-oleate precursor was completed and kept in N₂ at 150 °C until needed. Subsequently, 0.5 g of PbI₂ and 25 mL of ODE were mixed in a 100-mL three-neck flask at 120 °C for 10 min under vacuum. A preheated mixture of OA and OAm (130 °C, 2.5 mL each) was injected into the PbI₂ solution and the reaction flask was kept at 120 °C until a clear solution was formed. Then the reaction flask was heated to 185 °C under flowing N₂. Once 2 mL of the Cs-oleate precursor was immediately injected into the reaction flask, the mixture was quenched in an ice bath. After cooling to room temperature, the colloidal solution was mixed with 70 to 80 mL of MeOAc and then centrifuged at 7500 rpm for 5 min. The precipitated QDs were dispersed in 5 mL of hexane and re-precipitated by adding about 5 mL of MeOAc. After centrifugation (7500 rpm, 5 min), the resulting precipitate was redispersed in 15 mL of hexane and stored in refrigerator at 4 °C. To remove excess Cs-oleate and Pb-oleate, the QD solution was

centrifuged at 7500 rpm for 5 min after 24 hours of storage in refrigerator. The supernatant was filtered through a 0.45-μm nylon filter and ready for used.

FAPbI₃ QDs synthesis and purification. FAPbI₃ QDs was synthesized and purified following the previously reported method²⁶. The FA-oleate precursor was prepared by first degassing a mixture of 0.521 g of FA-acetate and 10 mL of OA in a 100-mL three-neck flask under a vacuum at 120 °C for 20 min. Then N₂ was introduced in the reaction flask and the clear reaction solution was yielded. After cooling to 90 °C, the FA-oleate precursor was kept in N₂ and ready for injection. To prepare PbI₂ solution, 0.344 g of PbI₂ was added into 20 mL of ODE and degassed at 120 °C for 20 min under vacuum in a 100-mL three-neck flask. A preheated mixture of OA and OAm (130 °C, 3 mL each) was injected into the PbI₂ solution and the reaction flask was kept at 120 °C until a clear solution was formed. Purging the flask with N₂, the PbI₂ solution was cooled down and kept at 80 °C. FA-oleate precursor (5 mL) was immediately injected into the PbI₂ solution. The mixture was quenched in an ice bath after 15 s. MeOAc (9 mL) was added into the colloidal solution after cooling to room temperature and then centrifuged at 8000 rpm for 30 min. The precipitated QDs was dispersed in 9 mL of toluene. Around 10 mL of MeOAc was added into the QDs solution and then it was centrifuged at 8000 rpm for 10 min. The resulting precipitate was redispersed in 10 mL of octane and stored in refrigerator at 4 °C for at least 24 h. Before use, the QDs solution was centrifuged at 7500 rpm for 5 min and the precipitate was decanted. The supernatant was filtered through a 0.45-μm nylon filter.

Preparation of Cs_{1-x}FA_xPbI₃ alloys. Colloidal solutions of CsPbI₃ and FAPbI₃ QDs were dispersed in octane, respectively. To obtain similar concentrations of these two solutions, the absorption spectra were measured, and each solution had a similar optical density near the band edge. After the concentrations were calibrated, these two colloidal solutions were mixed in different volume ratios to yield Cs_{1-x}FA_xPbI₃ QDs with the desired Cs/FA stoichiometry and then stored at room temperature for at least 48 h²⁶.

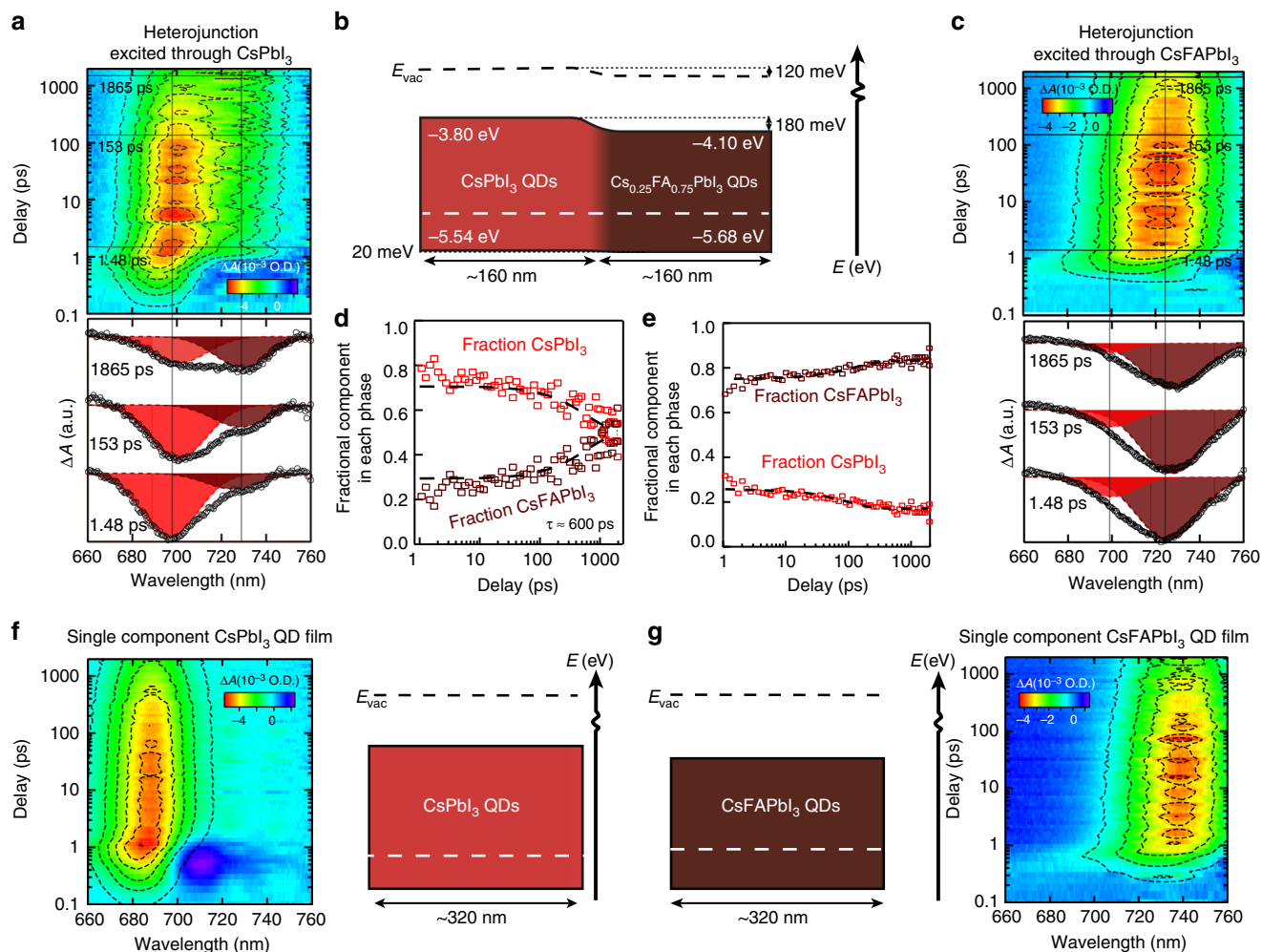


Fig. 4 Transient absorption of heterojunction QD films. **a** Pseudocolor image of transient response for QD heterostructure when photoexciting through the CsPbI₃ layer. For each of the surface plots with dashed contour lines one can visualize the carrier populations at various delay time delays between the pump and probe beam with the model described. Select cuts through the data are presented below the surface plots and offset vertically for clarity. Cuts are shown at 1.48 ps, 153 ps, and 1865 ps time delay. The spectra at each delay can be represented by the bleaching of two Gaussian peaks, one has a center wavelength at 697 nm (red-shaded Gaussian) and is associated with carriers occupying CsPbI₃ while the other peak has a center wavelength at 728 nm (brown-shaded Gaussian) and is associated with carriers spatially occupying the Cs_{0.25}FA_{0.75}PbI₃ component. Vertical lines show the position of the two centered components. **b** Energy level diagram of the heterostructured film with estimated band alignment from UPS. In experiment **a** light impinges from the left (CsPbI₃ QDs) while for **c** light impinges from the right (Cs_{0.25}FA_{0.75}PbI₃ QDs). From the alignment, electrons are driven to the FA-containing side with a conduction band offset of 180 meV while holes have a small (20 meV) offset driving holes toward CsPbI₃. **c** Pseudocolor image of transient response for QD heterostructure when photoexciting through the Cs_{0.25}FA_{0.75}PbI₃ layer. The coloring scheme of the decomposed spectra is the same as in **a**. **d, e** The decomposed fraction of the TA signal for each delay measured that arises from the CsPbI₃ (red-squares) and Cs_{0.25}FA_{0.75}PbI₃ (brown-squares) as a function of time when photoexciting through CsPbI₃ (**d**) or through Cs_{0.25}FA_{0.75}PbI₃ (**e**). For **d**, the fraction of CsPbI₃ decreases over time while Cs_{0.25}FA_{0.75}PbI₃ increases as electrons are transferred into the FA-containing layer with a charge transfer time average of around 600 ps. For **e**, the fraction of CsPbI₃ and Cs_{0.25}FA_{0.75}PbI₃ is analyzed after the first ps and then stay relatively unchanged. **f** Pseudocolor image (left) and diagram (right) of a thick single component CsPbI₃ film **g** Pseudocolor image (right) and diagram (left) of pure Cs_{0.25}FA_{0.75}PbI₃

Fabrication of QD films. Coupled Cs_{1-x}FA_xPbI₃ QD films (where $x = 0, 0.25, 0.50, 0.75,$ or 1.0) were deposited following previously reported methods²⁶ with slight modifications. Deposition of all QD films was carried out in a humidity-controlled box (relative humidity, 20–25%). First, saturated Pb(NO₃)₂ in MeOAc solution and FAI in EtOAc solution were prepared. Each layer of Cs_{1-x}FA_xPbI₃ QD was deposited by spin-coating at 1000 rpm for 20 s and 2000 rpm for 5 s. Subsequently, the film was swiftly soaked into the Pb(NO₃)₂ solution and then rinsed in the neat MeOAc solution. A total film with ~300 nm of thickness was obtained by repeating the process of spin-coating QDs and soaking in the solution four times. To achieve a heterojunction structure, Cs_{1-x}FA_xPbI₃ QDs with different Cs/FA stoichiometry was deposited by following different sequences. Finally, the film was dipped in FAI solution for 10 s and rinsed in the neat MeOAc solution^{10,12}.

Fabrication of PV devices. All of PV devices was fabricated by following previous literatures with slight modification^{10,11}. Patterned indium-doped tin oxide

(ITO) glass was cleaned by sonicating in isopropanol for 30 min and treated with UV-ozone for 5 min. An ~50 nm compact TiO₂ layer was deposited by spin-coating a clear solution of TiO₂ at 3000 rpm for 20 s; and then annealing at 450 °C for 30 min. The TiO₂ solution was synthesized by a sol-gel method from a precursor prepared by mixing 5 mL of EtOH, two drops of HCl, 125 mL of deionized water, and 375 mL of titanium ethoxide. The QD absorber layer was deposited following the procedure described above. Spiro-OMeTAD films were deposited by spin-coating at 5000 rpm for 30 s from a solution containing 72.3 mg spiro-OMeTAD, 28.8 μL 4-TBP and 17.5 μL of a bis(trifluoromethane)sulfonimide lithium salt (LiTFSI) stock solution (520 mg mL⁻¹ in acetonitrile) dissolved in 1 mL of chlorobenzene. All the spin-coating processes were carried out under ambient conditions unless otherwise specified. MoO_x was evaporated at a rate of 0.1 to 0.5 Å s⁻¹ at a base pressure lower than 2 × 10⁻⁷ torr, resulting in a total thickness of 15 nm. Al electrodes were deposited at a rate of 0.5 to 2.0 Å s⁻¹ for a total thickness of 200 nm. The encapsulation of devices was

processed in a N₂-filled glovebox by sealing the active area to another piece of glass with polyisobutylene tape.

Characterization of QD solutions and films. TEM images were obtained using a FEI Tecnai F20 electron microscope with 200 kV accelerating voltage. To determine elemental and isotopic distributions in solids, as well as the structure and composition of organic materials, time-of-flight secondary ion mass spectrometry (ToF-SIMS) is a powerful analytical technique to investigate HPSC materials and devices^{13,27}. An ION-ToF ToF-SIMS V spectrometer was utilized to depth-profile the Cs_{1-x}FA_xPbI₃ QD films. Analysis was carried out utilizing a 3-lens 30 kV BiMn primary ion gun, and the Bi₃⁺ primary-ion beam (operated in bunched mode; 21 ns pulse width, analysis current 0.7 pA) was scanned over a 25 × 25 micron area. Depth Profiling was completed with a 1 kV oxygen ion sputter beam (7 nA sputter current) rastered over a 150 × 150 micron area. All spectra during profiling were recorded at or below a primary ion dose density of 1 × 10¹² ions cm⁻² to remain at the static-sims limit.

Transient absorption spectra (TA) were recorded using a Continuum Integra-C laser, with an output of 800 nm at 1 kHz. The 800 nm beam was directed into a Palitra optical parametric amplifier to generate pump pulse (about 150 fs) at 400 nm and was modulated at 500 Hz through an optical chopper to block every other laser pulse. Femtosecond TA spectra were collected using Helios spectrometer (Ultrafast Systems). A small amount of 800 nm light was used to pump a sapphire crystal to create 450–800 nm probe light for TA.

For time-resolved microwave conductivity (TRMC) measurements, the perovskite QD films deposited onto pre-cleaned quartz substrates (1 cm × 2.5 cm × 1 mm) were photoexcited through the quartz side of the substrate with 650 nm (5 ns pulse width) pulses at 10 Hz from an optical parametric oscillator (Continuum Panther) pumped by the 355 nm harmonic of a Q-switched Nd:YAG laser (Continuum Powerlite). The transient change in photoconductance, $\Delta G(t)$, was recorded via transient change in the microwave power, $\Delta P(t)$, due to absorption of microwaves (ca. 9 GHz) by mobile photogenerated charge carriers in the sample. $\Delta G(t)$ was calculated by:

$$\Delta G(t) = \left(-\frac{1}{K}\right) \left(\frac{\Delta P(t)}{P}\right) \quad (1)$$

where K is a calibration factor experimentally determined from the dielectric properties of the QD films and the resonance characteristics of the microwave cavity. The end-of-pulse (peak) photoconductance, ΔG_{peak} , is related to the yield mobility product ($\varphi\Sigma\mu$) using the equation:

$$\Delta G_{\text{peak}} = \beta q_e N (\mu_e + \mu_h) = \beta q_e I_0 F_A \varphi \Sigma \mu \quad (2)$$

where $\beta = 2.2$ and is the ratio of the interior dimensions of the waveguide, φ is the yield of free-carrier generation, q_e is the electronic charge, N is the number of photogenerated charge-carrier pairs, μ_e and μ_h are the electron and hole mobilities (termed $\Sigma\mu$), I_0 is the incident photon flux of the excitation laser pulse, and F_A is the fraction of photons (650 nm) absorbed by the QD films. Pump excitation intensities were decreased until peak photoconductivity values and transient lifetime were intensity independent, provided sufficient signal-to-noise. At 650 nm, generation of charges can be uniform throughout the vertical cross section of the films, thus further mitigating higher-order recombination processes. Hence, we extracted the carrier mobilities of the QD films from this linear response region of the data.

XPS and UPS measurements were performed on a Kratos Axis Nova instrument, using monochromated Al-K α ($h\nu = 1486.7$ eV), and He-I ($h\nu = 21.22$ eV) excitation sources, respectively. The spectrometer binding-energy (BE) scale was calibrated by measuring valence-band and core-level spectra from sputter-cleaned Au and Cu foils ($E_F = 0.00$ eV, Au 4f_{7/2} = 83.96 eV, and Cu 2p_{3/2} = 932.62 eV)²⁸. XPS/UPS spectra were acquired at pass energy $E_{\text{pass}} = 20$ eV. The reference energy levels for spiro-OMeTAD and TiO₂ were taken from literature²⁹.

Characterization of PV devices. Devices were tested on a Newport Oriel Sol3A solar simulator with xenon lamp in the glove box at room temperature. The intensity of the solar simulator was calibrated to 100 mW cm⁻² AM1.5 G with a KG5 filtered Si reference solar cell that was certified by NREL PV Performance Characterization Team and the spectral mismatch factor was minimized to 0.9923. $J-V$ scans were measured from forward bias to reverse bias step and from reverse bias to forward (bias size: 100 mV, delay time: 10 ms, number of power line cycles: 0.1, respectively). The devices were masked with a black metal aperture to define an active area of 0.059 cm². The stabilized power output (SPO) of devices was measured by holding the illuminated devices at a constant voltage near the maximum power point of the $J-V$ scan and recording the continuous current output in the meantime. External quantum efficiency (EQE) measurements were performed utilizing a Newport Oriel IQE200.

To obtain the cross-sectional TEM images of devices, a Pt capping layer was deposited on the surface of devices to protect the thin-film structure. TEM foils were prepared by the standard focused ion beam (FIB) lift-out technique and then the final thickness was reduced to less than <100 nm by a Ga ion milling. To remove preparation damage on the TEM foils, a Fischione Nanomill was used and a low energy cleaning was carried out at 500 eV under vacuum of 10⁻⁷ torr at -170 °C for $\pm 10^\circ$. TEM observations were operated on a FEI Tecnai F20 TEM at

an acceleration voltage of 200 kV. Chemical analysis was performed with energy-dispersive X-ray spectrometry (EDS) in the high-angle annular dark-field (HAADF)-scanning TEM (STEM) mode.

Data availability

Data that support the plots within this work are available from the corresponding author upon reasonable request.

Received: 19 February 2019 Accepted: 20 May 2019

Published online: 28 June 2019

References

- Ning, Z. et al. Graded doping for enhanced colloidal quantum dot photovoltaics. *Adv. Mater.* **25**, 1719–1723 (2013).
- Haschke, J., Dupré, O., Boccard, M. & Ballif, C. Silicon heterojunction solar cells: recent technological development and practical aspects - from lab to industry. *Sol. Energy Mater. Sol. Cells* **187**, 140–153 (2018).
- Zhao, T. et al. Advanced architecture for colloidal PbS quantum dot solar cells exploiting a CdSe quantum dot buffer layer. *ACS Nano* **10**, 9267–9273 (2016).
- Adinolfi, V. et al. Electric field engineering using quantum-size-effect-tuned heterojunctions. *Appl. Phys. Lett.* **103**, 011106 (2013).
- Crisp, R. W. et al. Metal halide solid-state surface treatment for high efficiency PbS and PbSe QD solar cells. *Sci. Rep.* **5**, 9945 (2015).
- Etgar, L., Gao, P., Qin, P., Graetzel, M. & Nazeeruddin, M. K. A hybrid lead iodide perovskite and lead sulfide QD heterojunction solar cell to obtain a panchromatic response. *J. Mater. Chem. A* **2**, 11586–11590 (2014).
- Luque, A. L. & Viacheslav, A. in *Concentrator Photovoltaics* (eds Luque, A. L. & Viacheslav, A.) 25–50 (Springer, Berlin, Heidelberg, 2007).
- Jiang, C.-S. et al. Direct evidence of a buried homojunction in Cu(In,Ga)Se₂ solar cells. *Appl. Phys. Lett.* **82**, 127–129 (2002).
- Strohm, A. et al. ZnO/InxSy/Cu(In,Ga)Se₂ solar cells fabricated by coherent heterojunction formation. *Thin Solid Films* **480–481**, 162–167 (2005).
- Sanehira, E. M. et al. Enhanced mobility CsPbI₃ quantum dot arrays for record-efficiency, high-voltage photovoltaic cells. *Sci. Adv.* **3**, ea04204 (2017).
- Swarnkar, A. et al. Quantum dot-induced phase stabilization of α -CsPbI₃ perovskite for high-efficiency photovoltaics. *Science* **354**, 92–95 (2016).
- Wheeler, L. M. et al. Targeted ligand-exchange chemistry on cesium lead halide perovskite quantum dots for high-efficiency photovoltaics. *J. Am. Chem. Soc.* **140**, 10504–10513 (2018).
- Harvey, S. P. et al. Probing perovskite inhomogeneity beyond the surface: TOF-SIMS analysis of halide perovskite photovoltaic devices. *ACS Appl. Mater. Interfaces* **10**, 28541–28552 (2018).
- Zolfaghari, Z. et al. Operation mechanism of perovskite quantum dot solar cells probed by impedance spectroscopy. *ACS Energy Lett.* **4**, 251–258 (2019).
- Bian, H. et al. Graded bandgap CsPbI_{2-x}Br_{1-x} perovskite solar cells with a stabilized efficiency of 14.4%. *Joule* **2**, 1500–1510 (2018).
- Moriarty, T. & Levi, D. in *Proc. 2017 IEEE 44th Photovoltaic Specialist Conference (PVSC)* 483–486 (IEEE, Washington, DC, USA, 2017).
- Zimmermann, E. et al. Characterization of perovskite solar cells: Towards a reliable measurement protocol. *APL Mater.* **4**, 091901 (2016).
- Park, S. H. et al. Bulk heterojunction solar cells with internal quantum efficiency approaching 100%. *Nat. Photon.* **3**, 297 (2009).
- Chen, X., Lu, H., Yang, Y. & Beard, M. C. Excitonic effects in methylammonium lead halide perovskites. *J. Phys. Chem. Lett.* **9**, 2595–2603 (2018).
- Calik, M. et al. Extraction of photogenerated electrons and holes from a covalent organic framework integrated heterojunction. *J. Am. Chem. Soc.* **136**, 17802–17807 (2014).
- Lan, X., Masala, S. & Sargent, E. H. Charge-extraction strategies for colloidal quantum dot photovoltaics. *Nat. Mater.* **13**, 233 (2014).
- Wu, K. et al. Ultrafast interfacial electron and hole transfer from CsPbBr₃ perovskite quantum dots. *J. Am. Chem. Soc.* **137**, 12792–12795 (2015).
- Hu, Y. et al. Hybrid perovskite/perovskite heterojunction solar cells. *ACS Nano* **10**, 5999–6007 (2016).
- Cui, P. et al. Planar p–n homojunction perovskite solar cells with efficiency exceeding 21.3%. *Nat. Energy* **4**, 150–159 (2019).
- Protesescu, L. et al. Nanocrystals of cesium lead halide perovskites (CsPbX₃, X = Cl, Br, and I): novel optoelectronic materials showing bright emission with wide color gamut. *Nano Lett.* **15**, 3692–3696 (2015).
- Hazarika, A. et al. Perovskite quantum dot photovoltaic materials beyond the reach of thin films: full-range tuning of A-site cation composition. *ACS Nano* **12**, 10327–10337 (2018).
- Christians, J. A. et al. Tailored interfaces of unencapsulated perovskite solar cells for >1,000 h operational stability. *Nat. Energy* **3**, 68–74 (2018).

28. Seah, M. P., Gilmore, I. S. & Beamson, G. XPS: binding energy calibration of electron spectrometers 5—re-evaluation of the reference energies. *Surf. Interface Anal.* **26**, 642–649 (1998).
29. Jiménez-López, J., Cambarau, W., Cabau, L. & Palomares, E. Charge injection, carriers recombination and HOMO energy level relationship in perovskite solar cells. *Sci. Rep.* **7**, 6101 (2017).

Acknowledgements

This work was authored by Alliance for Sustainable Energy, LLC, the manager and operator of the National Renewable Energy Laboratory for the U.S. Department of Energy (DOE) under contract no. DE-AC36-08GO28308. We acknowledge the Department of Defense Operational Energy Capability Improvement Fund (OECIF) for development of these QD solar cells. Transient absorption work is supported from the Center for Hybrid Organic Inorganic Semiconductors for Energy (CHOISE) an Energy Frontier Research Center funded by the Office of Basic Energy Sciences, Office of Science within the U.S. Department of Energy. Q.Z. acknowledges fellowship support from the China Scholarship Council and Natural Science of Foundation China (21576140). The views expressed in the article do not necessarily represent the views of the DOE or the U.S. Government.

Author contributions

Q.Z. and J.M.L. conceived the project, analyzed all data, and wrote the first draft. Q.Z. fabricated the devices and prepared samples for measurements. Q.Z. prepared quantum dots under the guidance of A.H. X.C. constructed the TA experimental set-up and performed the TA measurements. M.C.B. analyzed TA data. S.P.H. performed ToF-SIMS measurements and analyzed the data. G.R.T. carried out XPS and UPS measurements and film energetics simulation and analyzed the data. B.W.L. performed TRMC measurements. J.L. and C.X. performed imaging measurements. Q.Z. encapsulated devices under the guidance of T.S. and L.S. J.M.L. supervised the entire project. G.L.

and M.Z. discussed all results. All authors contributed to the final writing of the manuscript.

Additional information

Supplementary Information accompanies this paper at <https://doi.org/10.1038/s41467-019-10856-z>.

Competing interests: The authors declare no competing interests.

Reprints and permission information is available online at <http://npg.nature.com/reprintsandpermissions/>

Peer review information: *Nature Communications* thanks Weijie Zhao and other anonymous reviewer(s) for their contribution to the peer review of this work.

Publisher's note: Springer Nature remains neutral with regard to jurisdictional claims in published maps and institutional affiliations.



Open Access This article is licensed under a Creative Commons Attribution 4.0 International License, which permits use, sharing, adaptation, distribution and reproduction in any medium or format, as long as you give appropriate credit to the original author(s) and the source, provide a link to the Creative Commons license, and indicate if changes were made. The images or other third party material in this article are included in the article's Creative Commons license, unless indicated otherwise in a credit line to the material. If material is not included in the article's Creative Commons license and your intended use is not permitted by statutory regulation or exceeds the permitted use, you will need to obtain permission directly from the copyright holder. To view a copy of this license, visit <http://creativecommons.org/licenses/by/4.0/>.

© The Author(s) 2019